

## Supplementary information

### Photocatalytic hydrogen evolution activity of Co/CoO hybrid structure : a first-principle study on Co layer thickness effect

Kyoung-Won Park<sup>1,2</sup>, Alexie M. Kolpak<sup>3,\*</sup>

1. Department of Materials Science and Engineering, Massachusetts Institute of Technology, Cambridge, Massachusetts 02139, USA

2. Center for Biomaterials, Korea Institute of Science and Technology (KIST), Seoul, 02792, Republic of Korea

3. Department of Mechanical Engineering, Massachusetts Institute of Technology, Cambridge, Massachusetts 02139, USA

#### Corresponding Author

\* alexie.kolpak@gmail.com

## Example of atomic configuration of Co/CoO(111) supercell

Fig. S1 shows an example of an atomic configuration of the Co( $x$ )/CoO(111) supercell relaxed with DFT calculation. As explained in the main text, the initial structure of the Co(2)/CoO(111) was constructed by removing two oxygen atomic layers from both the top and bottom of the initial CoO(111) supercells as shown in Fig. S1.

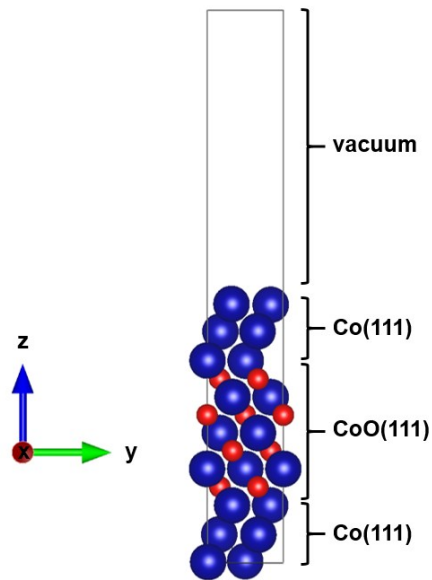


**Fig. S1** Atomic configuration of the Co(2)/CoO(111) symmetric supercell, relaxed with DFT calculation.

## Hartree potential of water/Co/CoO(111)

Fig. S2(a) shows an example of water/Co/CoO(111) supercell constructed in this study for the calculation of the potential drop at the interface of the Co/CoO(111) hybrid structure and water. The separately relaxed Co(2)/CoO(111) symmetric slab and liquid bulk water are positioned in contact with each other as shown in Fig. S2(a) as an example. The calculated planar averaged Hartree potential of the water/Co(2)/CoO(111) structure is plotted as a function of position in Fig. S2(b).

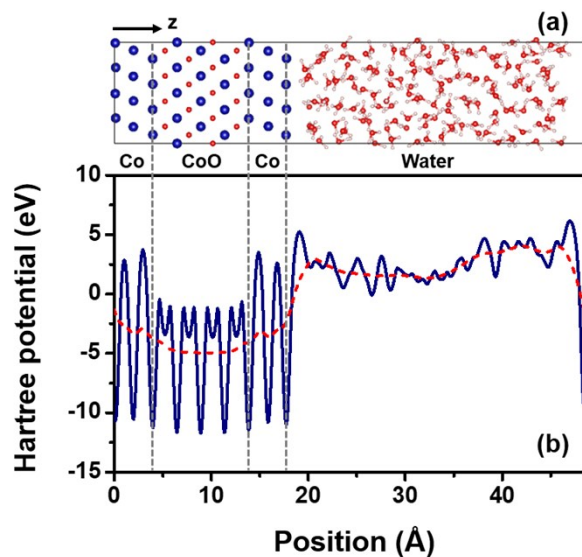


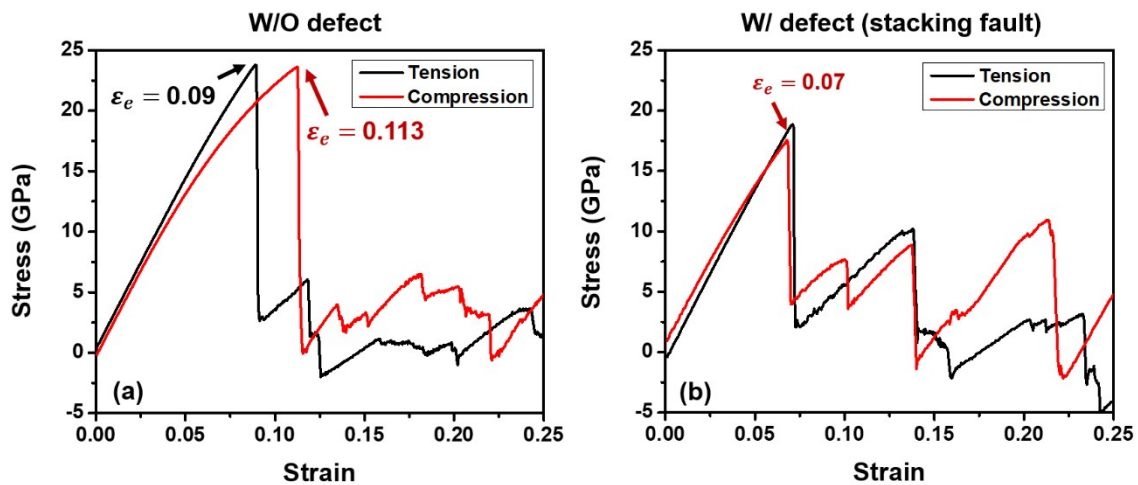
**Fig. S2(a)** Snapshot of the atomic distribution of the water/Co(2)/CoO(111) interface. Blue, red, and white circles indicate Co, O, and H atoms, respectively. **(b)** Planar-averaged Hartree potential of the water/Co(2)/CoO(111) interface computed for the structure shown in (a). Dotted red line in (b) indicates macro-averaged Hartree potentials obtained using the approach in Ref. 1.

# Mechanical properties of FCC-Co

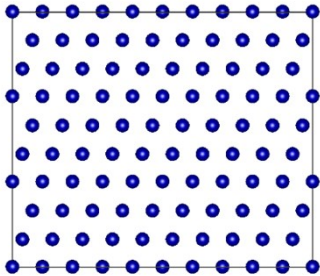
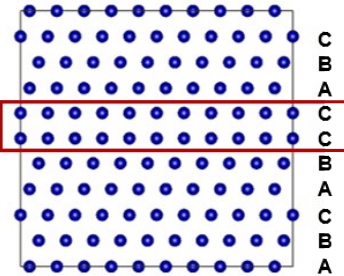
## 1) Defect effect

Fig. S3(a) shows stress-strain curves obtained during uniaxial compression and tension of a defect-free supercell of FCC-Co. The perfect supercell exhibits about 9% elastic limit for tension and 11.3% for compression, with yield strength of  $\sim 23$  GPa. However, the elastic limit significantly decreases to  $\sim 7\%$  for both compression and tension in the supercell containing a stacking-fault (Fig. S3(b)). The significant decrease in the elastic limit due to the presence of defect, is interpreted as the reason why the elastic limit in the real experimental measurement is very low (offset yield point :  $\sim 0.2\%$ ), unlike the present calculation: the presence of structural defects including stacking-fault, dislocation and void etc., make materials yield at the very lower elastic limit as well as the strength compared to the theoretical values. Therefore, the defect-free supercell can have the very high yield strength (in the range of GPa) close to the theoretical strength as observed in Fig. S3, unlike the normal range observed experimentally (in the range of MPa).

In addition, Young's modulus of Co obtained from the stress-strain curves is about 200 GPa for both the perfect and defect-containing supercell, similar to the experimentally measured value (209 GPa [2]). This means the physical properties related to atomic bond strength are not significantly affected by the presence of the defect. Therefore, in a real experimental measurement, although Young's modulus does not change much with and without the presence of a defect, elastic limit and yield strength show very lower values compared to the theoretical values.

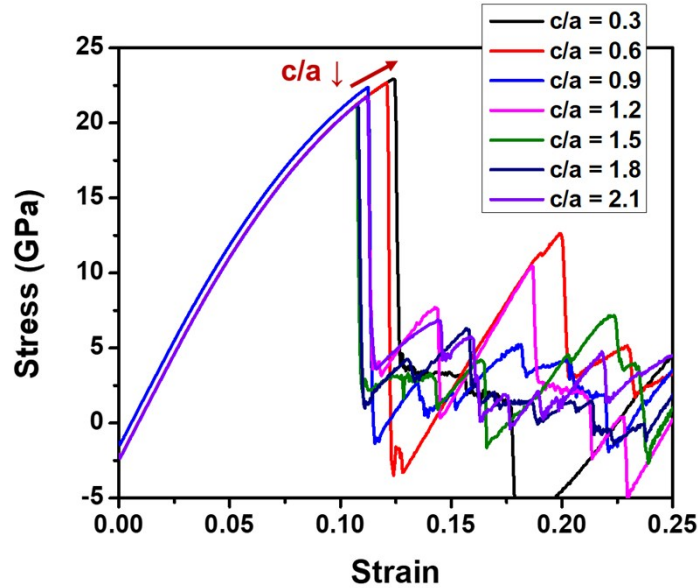


**Fig. S3** Stress-strain curves of **(a)** a perfect supercell of FCC-Co and **(b)** a FCC-Co supercell containing a stacking-fault.

<b>MD simulation method</b>		
Using the classical MD simulation technique, FCC-Co was modeled by employing the EAM (Embedded Atom Method) potential [2] and using the large-scale atomic/molecular massively parallel simulator (LAMMPS) code [3]. Periodic boundary conditions were applied to the three-dimensional (3-D) directions in order to eliminate the surface effects. FCC-Co supercells were relaxed for 50 ps using NVT ensemble at 10K. Subsequently, uniaxial tensile (or compressive) strain was imposed on the supercells at a rate of $5 \times 10^8/s$ at 10K.		
	<b>FCC-Co w/o defect (in Fig. S3(a))</b>	<b>FCC-Co w/ defect (in Fig. S3(b))</b>
<b>Aspect ratio (a/c) of a supercell</b>	0.9	1.0
<b>Number of atoms</b>	900	1000
<b>Supercell size</b>	$25 \times 22 \times 18.5 \text{ \AA}^3$	$25 \times 22 \times 20.5 \text{ \AA}^3$
<b>Cell configuration</b>		

## 2) Aspect ratio effect

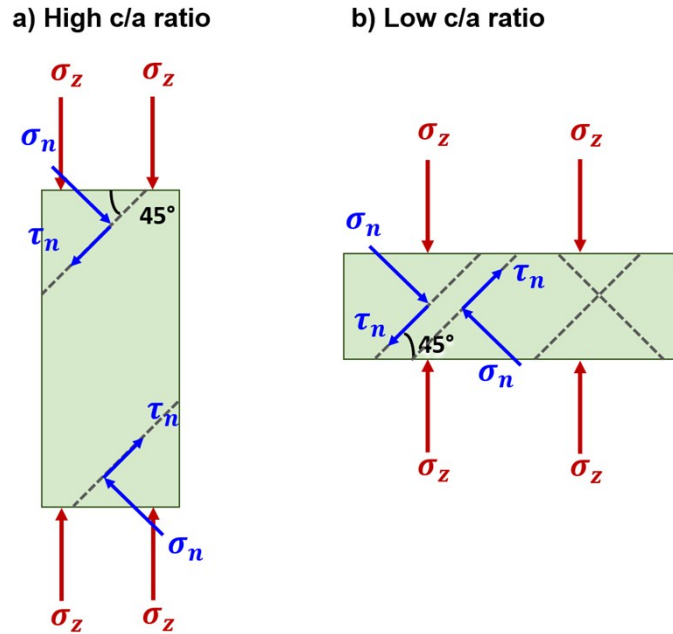
Fig. S4(a) shows stress-strain curves obtained during compressive strain of FCC-Co, with variation of aspect ratio of the Co supercell from 0.3 to 2.1. The MD simulation was performed in the same condition as for Fig. S3 except for the varied height of the supercell (with the fixed area of the supercell but different aspect ratio). With decreasing the aspect ratio of the supercell (going closer to thin film structure), the elastic limit increases. This difference is caused by the different stress states subjected to the supercells with different aspect ratio as schematically illustrated in Fig. S4(b).



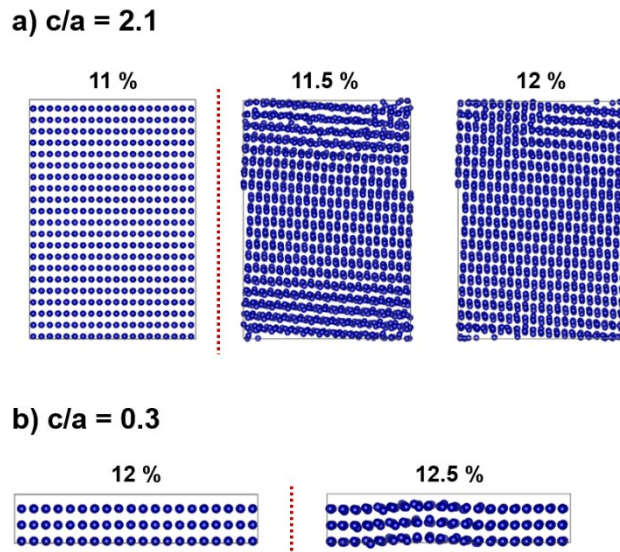
**Fig. S4** Stress-strain curves of perfect supercells of Co with variation of aspect ratio (0.3–2.1)

Fig. S5 shows the schematics depicting the stress states exerting on the samples with different aspect ratios. Uniaxial stress is decomposed into the normal stress and the maximum shear stress in the plane that is inclined at  $45^\circ$  with respect to the direction of the uniaxial stress. Shear stress is known to play a crucial role in the structural changes of metals. In the case of high aspect ratio close to the general experimental mechanical deformation test condition (Fig. S5(a)), the shear stress coming from the uniaxial stress, mainly exerts on the side of height direction. The shear stress over the yield point induces the permanent atomic displacement from the original location by sliding along the shear plane as shown in Fig. S6(a). The deformation behavior shown in Fig. S6(a) follows the typical plastic deformation of bulk metals.

However, in the structure of low aspect ratio (Fig. S5(b)), the shear stress originated from uniaxial compressive stress acting on the upper and bottom sides of the sample interact with each other, but with opposite directions. Thus, some part of the shear stress can be canceled, and eventually, the actual stress acting on the shear plane can be smaller than the externally applied stress from the uniaxial stress. Therefore, the structure with low aspect ratio (similar to thin film) can sustain more severe external stress and elastic strain compared to the structure with high aspect ratio as observed in Fig. S4. Even beyond the yield point (Fig. S6(b)), buckling phenomenon is observed, which suggests that thin film becomes ductile unlike the structure of the high aspect ratio.



**Fig. S5** Schematics of stress states exerting on samples (a) with low aspect ratio and (b) with high aspect ratio under uniaxial compression.  $\sigma_n$  and  $\tau_n$  denote normal and shear stress acting on shear plane when the plane is subject to the maximum shear strain along 45 degrees of the uniaxial compressive stress ( $\sigma_z$ ). If uniaxial tension is exerting on the same samples, the direction of the normal stress would be the other direction (pointing out from the shear plane).



**Fig. S6** Snapshots of atomic configuration in FCC-Co supercells with aspect ratio,  $c/a =$  (a) 2.1 and (b) 0.3, under compressive deformation. The number at the top of each figure denotes the applied engineering strain

(%). The vertical red dotted lines are to separate before and after the yielding; the left side of the red line is before yielding, the right side is beyond the yield point.

### 3) Size effect

Fig. S7 shows the size effect on the elastic limit and yield strength of FCC-Co. As the supercell size decreases (1/5 length of the larger structure), the elastic limit and yield strength increase, even though the two supercells have the same aspect ratio. Since there is no change in the atomic bond strength between Co atoms, Young's modulus is independent of the supercell size. This means high strength and elasticity close to the theoretical values can be achieved by the size reduction as frequently observed experimentally.

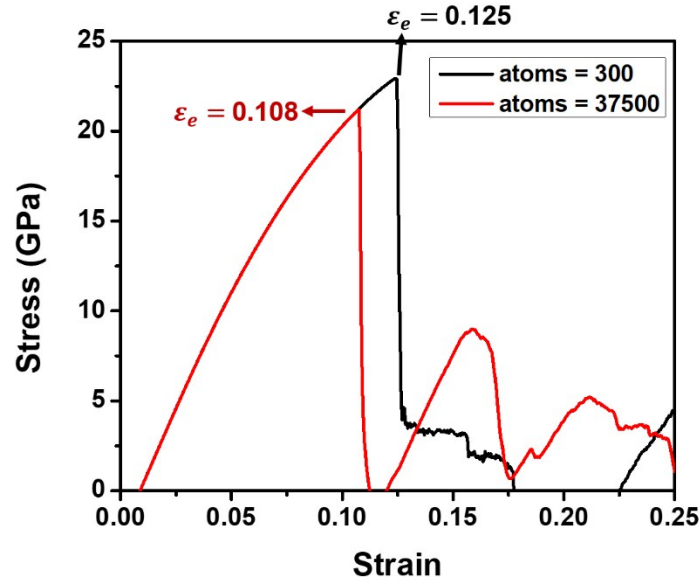


**Fig. S7** Stress-strain curves of FCC-Co supercells composed of 300 (black line) and 37500 Co atoms (red line) with the same aspect ratio = 0.3.

### Work function change with strain and Co layer thickness

Fig. S8 shows work function of FCC-Co(111) slabs under 20% tensile strain along the in-plane direction (Co-20%, red circle), as a function of Co layer thickness. Along the out-of-plane axis, compressive strain following Poisson's ratio is applied by changing the lattice distance.



The work functions of 1 – 5 atomic layered Co slabs do not show a big difference among them, around 4.1 eV, unlike the work functions of the undeformed FCC-Co(111) slabs (IU-Co, green square). The pristine FCC-Co(111) slabs show a monotonic increase in work function with increasing the Co thickness, as shown in the main text. Therefore, although tensile in-plane strain decreases the work function of the FCC-Co(111) slabs, the amount of the decrease is dependent on the slab thickness. The rough tendency shows that the work function largely decreases as the thickness of the FCC-Co(111) slab increases, by the in-plane tensile strain.

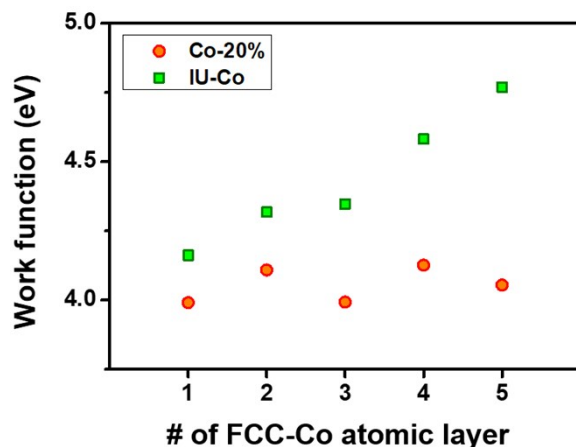


**Fig. S8** Work functions of pristine FCC-Co(111) slabs (IU-Co, green square) and of FCC-Co(111) slabs under 20% tensile strain along the in-plane direction (Co-20%, red circle), with respect to Co layer thickness.

### Work function change with strain

Fig. S9 shows the variation of work function of the FCC-Co(111) slab as a function of the in-plane strain. The supercell is composed of 5 atomic layers parallel to the (111) planes, together with vacuum layer of  $\sim 15$  Å. The in-plane strain is applied to the FCC-Co(111) lattice along both  $x$ - and  $y$ -axis, and the out-of-plane strain perpendicular to the thickness direction ( $z$ -axis) is also applied by the strain determined by Poisson's ratio of Co. As can be seen in Fig. S9, work function of the FCC-Co(111) slab decreases as larger tensile strain is applied along the in-plane direction, while it enhances with increasing the compressive strain.

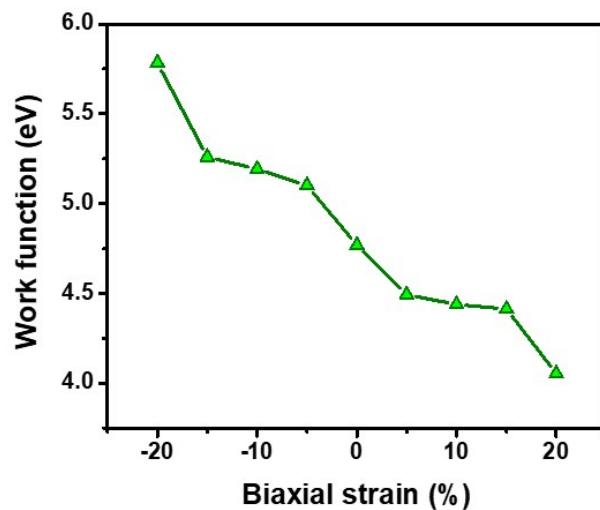


**Fig. S9** Variation in work function of FCC-Co(111) slab with respect to the in-plane strain. Negative strain denotes compressive strain, while positive one is tensile strain.

### Schematic of charge state

Fig. S10 shows the relative amount/direction of electron transfer across the interface of Co/CoO(111) structure with different Co layer thickness, which determines the band bending aspects in the CoO layers. As the Co layer becomes thicker (or thinner), electrons move to the Co layer (or CoO layer) in the process of the electrochemical potential equilibration, making the CoO layer more positively charged as schematically depicted in Fig. S10. Therefore, the degree of upward (or downward) band bending increases (or decreases) with increasing the Co layer thickness. These Co layer thickness-dependent band bending aspects and charge states of the Co/CoO(111) structures are mainly affected by the relative electron affinities of the Co and CoO layers, which are estimated with work functions of the Co and CoO layers as explained in the main text.

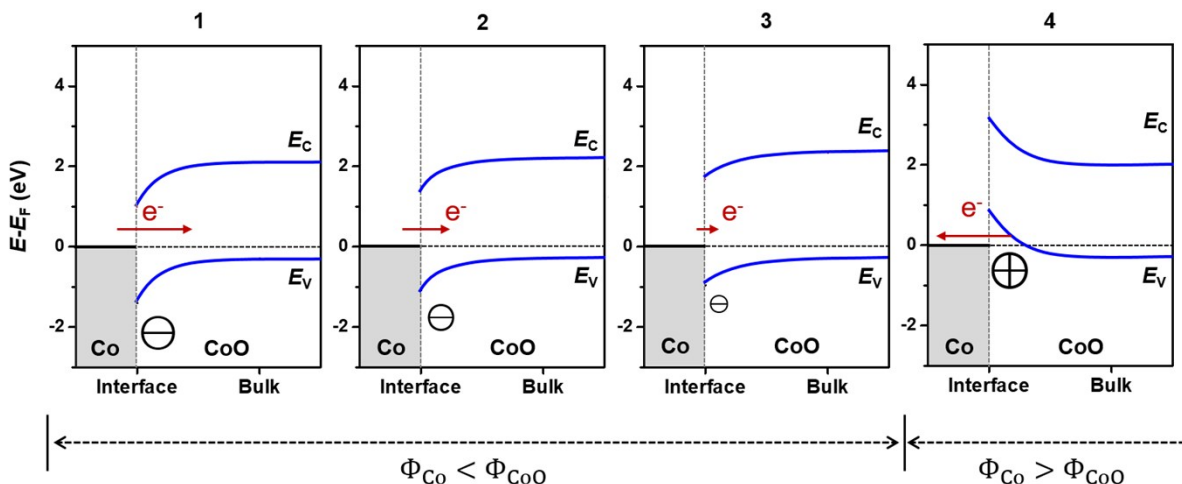


**Fig. S10** Schematic depicting charge states of CoO layer in Co(x)/CoO(111) hybrid structures, determined by electron transfer process in the electrochemical equilibration process. The process and charge state are explained on band bending diagrams of Co(x)/CoO(111) hybrid structures (shown in the main text). The number at the top of each graph denotes  $x$  in the Co(x)/CoO(111) structures. The red arrows in the figures are the direction/amount of electron transfer in the process of electrochemical potential equilibration.

### Choice of core-shell structure for lower HER overpotential

To understand the effect of core-shell structures on HER activity, we classify the Co/CoO core-shell structures into type-I and type-II as shown in Fig. S11. The type-I structure has the Co layer in the shell, and the CoO layer in the core. The type-II structure has the Co layer in the core, and the CoO layer in the shell. Fig. S11 shows the free energy change for hydrogen adsorption ( $\Delta G_{H^*}$ ) of the two kinds of Co/CoO(111) core-shell structures, calculated with DFT. The Co/CoO(111) core-shell structures have different Co layer fractions. Most of the Co/CoO structures have negative  $\Delta G_{H^*}$  values, which means hydrogen strongly binds with the Co/CoO structures. As a function of the Co layer fraction in the structures, the  $\Delta G_{H^*}$  value shows parabolic change both in type-I and -II, which shows the minimum HER overpotential in the middle of the Co layer fraction. This indicates that there is an optimal Co layer fraction for efficient hydrogen evolution. Between the type-I and type-II structures, the type-I structure has lower HER overpotential than the type-II structure independent of the Co layer fraction as can be seen in Fig. S11. Hence, hydrogen evolution is expected to be easier on the type-I structure than on the type-II structure, and predominantly occurs on the type-I structure.

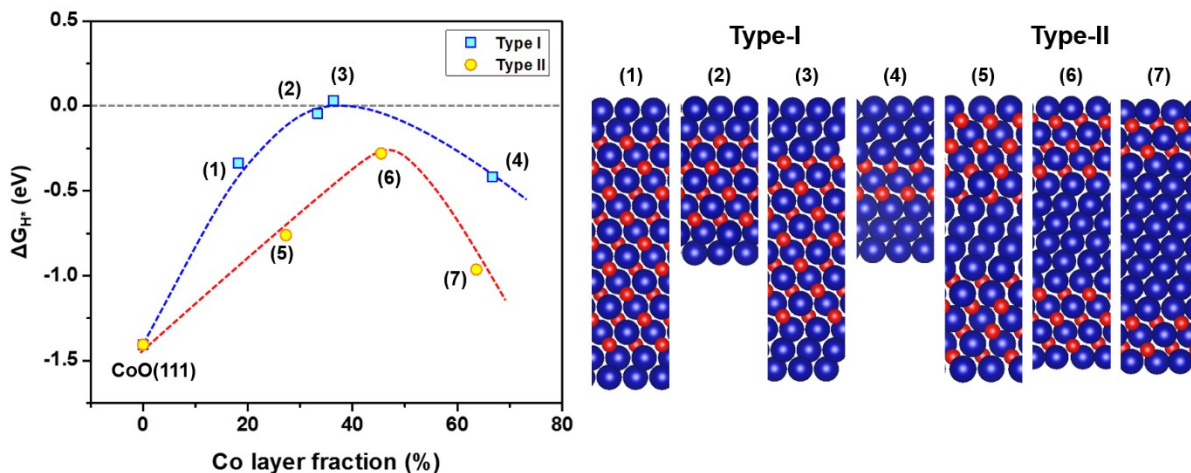


**Fig. S11** Left : Free energy change for hydrogen adsorption ( $\Delta G_{H^*}$ ) of type-I and -II Co/CoO(111) core-shell structure with respect to Co layer fraction (at pH = 0). Right : Atomic configurations of the Co/CoO(111) core-shell symmetric supercells of the type-I and -II used for the calculations of the  $\Delta G_{H^*}$  values in the left figure.

## Electron exchange between H/Co/CoO and binding strength

To quantify the electron exchange between the Co/CoO surfaces and the adsorbed hydrogen, and the relationship between the electron exchange and the  $\Delta G_{H^*}$  (or HER overpotential), we investigate the local density of states (LDOSs) of the outermost surface Co layers both in the Co(x)/CoO(111) structures (blue lines) and in the H-adsorbed Co(x)/CoO(111) structures (orange lines), as shown in Fig. S12. The reason for the selection of only the outermost surface is based on the idea that if there is an electron exchange between the surface and H in the process of adsorption, the exchange actively occurs on the outermost surface, that is, the surface Co layer.

The LDOSs of the Co layers in the Co(1)/CoO(111) and Co(2)/CoO(111) structures show no big difference between the LDOSs of the bare and the H-adsorbed Co/CoO(111) structures, suggesting that the two structures rarely exchange electrons with H, in the process of H adsorption. With the ignorable electron exchange, H adsorption-desorption readily occurs on the thin Co decorated hybrid structures, therefore, the very low HER overpotentials observed in the Co(1)/CoO(111) and Co(2)/CoO(111) structures (Fig. 4(b) in the main text) are possible. We think that the state with the very low  $\Delta G_{H^*}$  value is the well-balanced bonding state for efficient hydrogen evolution on the Co/CoO(111) surfaces.

On the other hand, the Co(3)/CoO(111) structure shifts the LDOS of the Co layer to lower energy with H adsorption, which means electrons occupy more energy states in the Co layer after the H adsorption. This implies that H binds with the Co(3)/CoO(111) structure more strongly with a larger negative value of  $\Delta G_{H^*}$  (Fig. 4(b) in the main text), by the electron transferred from H.

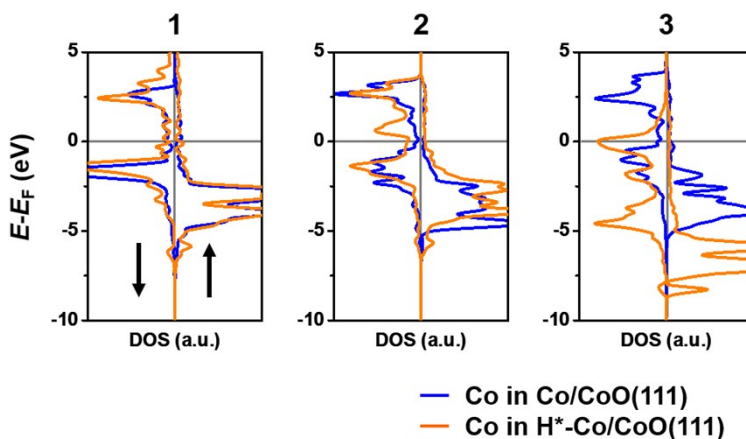


**Fig. S12** Local density of states (LDOSs) of the outmost surface Co layers in Co( $x$ )/CoO(111) structures (blue lines) and in the H-adsorbed Co( $x$ )/CoO(111) structures (orange lines). Number at the top of each graph denotes the number of Co layers ( $x$ ) in the Co( $x$ )/CoO(111) hybrid structures.

### ***Ab initio* MD of Co(1)/CoO(111), RS-CoO(111) and FCC-Co(111)**

Fig. S13 shows the snapshots of the initial and *ab initio* MD relaxed water/Co(1)/CoO(111) structure at 298K. The Co(1)/CoO(111) surface spontaneously dissociates water into OH and H, near the surface. The created OHs are adsorbed on the Co(1)/CoO(111) surface, while some Hs are desorbed from the surface, finally forming an H<sub>2</sub> molecule. Although bare RS-CoO(111) surface can dissociate water into OH and H (Fig. S14(a)), H<sub>2</sub> does not form on the CoO(111) surface. Instead, the OH and H are adsorbed on the surface. FCC-Co(111) is unable to cleave water molecules and water molecules keep their intact state (Fig. S14(b)).

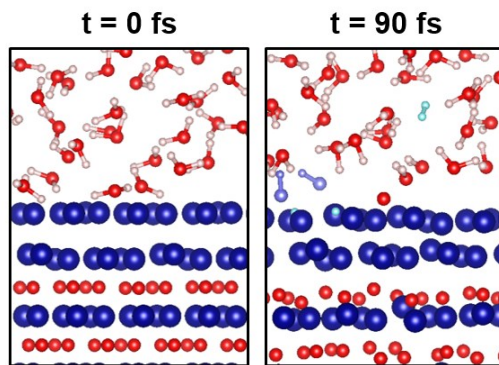


**Fig. S13** Initial and *ab initio* MD relaxed atomic configurations of Co(1)/CoO(111) hybrid structure, in direct contact with water molecules at 298 K. Blue, red, white circles denote Co, O, H. Light Purple and sky blue indicate OH and H which are formed by the dissociation of water on the surface. The H-H bond (sky blue) on the upper right side, indicates the formation of H<sub>2</sub>.

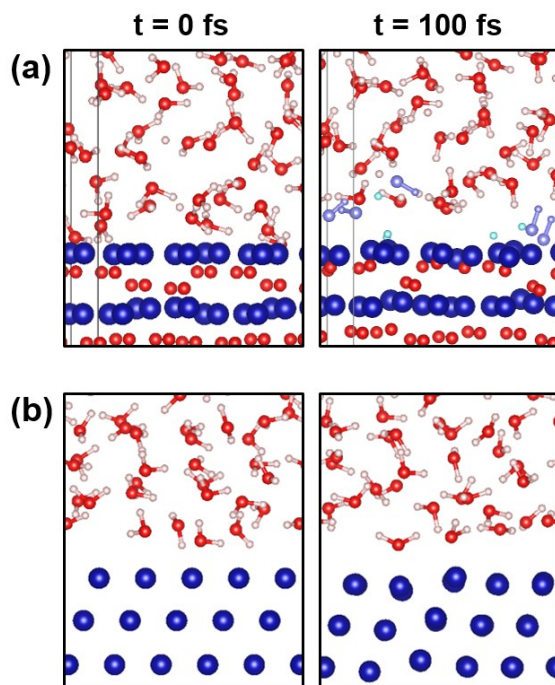


**Fig. S14** Initial and *ab initio* MD relaxed atomic configurations of (a) bare CoO(111) and (b) FCC-Co(111), in direct contact with water molecules at 298 K. Blue, red, white circles denote Co, O, H. Light purple and sky blue indicate OH and H which are formed by the dissociation of water on the surface.

## Transition state of HER vs. energy of hot electrons

To understand whether the created hot electrons in the Co layers have energies high enough to overcome the kinetic barriers for HER and induce the reaction, we compare the Fermi level ( $E_F$ ) of the  $\text{Co}(x)/\text{CoO}(111)$  structure with the transition state ( $E_{TS}$ ) of the HER which is directly related to the kinetic barrier, as shown in Fig. S15. The kinetic barrier is estimated from free energy change for hydrogen adsorption ( $\Delta G_{H^*}$ ), as explained in the main text. Since the created hot electrons in metal have energies higher than the  $E_F$ , if the  $E_F$  of the  $\text{Co}(x)/\text{CoO}(111)$  structure is above the kinetic barrier for HER, hydrogen is expected to be created on the Co layers in the  $\text{Co}(x)/\text{CoO}$  hybrid structure, with the SPR effect.

As can be seen in Fig. S15, the  $E_F$ s of the  $\text{Co}(x)/\text{CoO}(111)$  structures are above the  $E_{TS}$  for the HER, which suggests that all hot electrons generated in the Co layers in the structures, can induce the HER, and evolve hydrogen on the hybrid structures.

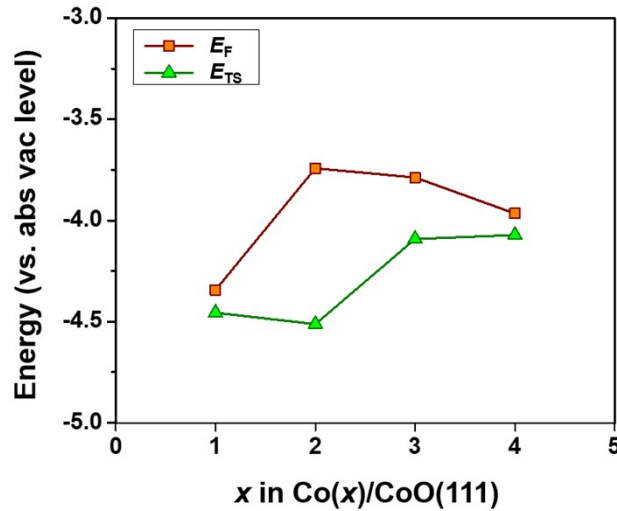


**Fig. S15** Energy of the Fermi level and transition state of  $\text{Co}(x)/\text{CoO}(111)$  hybrid structures, where  $x$  is the number of Co layers. The calculated energy of the Fermi level ( $E_F$ ) and transition state ( $E_{TS}$ ) is plotted in reference to the absolute vacuum level ( $E = 0$ ).

## References

- [1] A. Baldereschi, S. Baroni and R. Resta, *Phys. Rev. Lett.*, 1988, **61**, 734.
- [2] R. Passianot and E.J. Savino, *Phys. Rev. B*, 1992, **45**, 12704.
- [3] S. Plimpton. *J. Comp. Phys.*, 1995, **117**, 1.